Ultrathin a-Si:H/Oxide Transparent Solar Cells Exhibiting UV-Blue Selective-Like Absorption

Alex J. Lopez-Garcia,* Cristobal Voz, Jose Miguel Asensi, Joaquim Puigdollers, Víctor Izquierdo-Roca, and Alejandro Pérez-Rodríguez

Herein, the fabrication of transparent solar cells based on nanometric (8 and 30 nm) intrinsic hydrogenated amorphous silicon films (a-Si:H) and using oxide thin films as transparent carrier selective contacts are reported. The ultrathin devices present photovoltaic effect and high average visible transmittance (AVT). Additionally, they display a shifted spectral response toward short wavelengths. Glass/fluorine-doped tin oxide (FTO)/aluminum-doped zinc oxide (AZO)/a-Si:H/MoO$_3$/indium tin oxide (ITO) prototypes are shown, presenting AVT = 35% and photovoltaic conversion efficiency (PCE) = 2% for a device with a 30 nm a-Si:H film. This yields a light utilization efficiency (LUE) of 0.7%, a record up to this date for inorganic oxide-based transparent solar cells. For devices including an 8 nm a-Si:H film, the AVT reaches 66% with a PCE = 0.6% (LUE = 0.4%). These high AVT values are comparable or even superior in some cases to those achieved for pure oxide devices. These findings confirm the potential of the proposed architectures for the development of highly transparent energy harvesters as functional components in building-integrated photovoltaics (BIPV), agrophotovoltaics (APV), sensors and other low-power devices. In addition, these devices are fabricated with earth-abundant materials and with up-scalable techniques that can allow for a feasible implementation.

1. Introduction

Up to this date, the photovoltaic (PV) landscape shows a clear dependency on first-generation c-Si solar modules (and some second-generation thin-film technologies such as CdTe or copper indium gallium sulfide (CIGS)), with a clear aim toward high-efficiency and high-power production. As so, the implementation of such renewable energy sources has been focused on the deployment of solar farms. In the last decades, overall costs have greatly decreased and in many countries, applications of tariffs have allowed for an even further decrease in costs, allowing the solar technologies to span toward everyday user consumption. Examples of these are typical rooftop installations at home that allow users to auto-consume by having on-site energy generation.[1]

One of the key disadvantages of commercial PV technologies is that their implementation and output power are surface area dependent, among other issues such as high weight, use of relatively large amounts of critical raw materials, and in some cases toxic precursors. This poses an important limitation for conventional PV as many surfaces that are available (e.g., in buildings' façades) cannot be exploited by such technologies. Additionally, in constructions and utilities, there is also a demand to keep certain aesthetics of the surfaces or grazing elements that brings additional limitations for massive and decentralized deployment of solar technologies. To be able to use the available surfaces of façades, sensors, windows, or shading elements (amongst others) for ubiquitous on-site power generation and to allow for distributed applications, it is important to develop alternative concepts.

Transparent photovoltaic (TPV) is a clear example of how the field of PVs is shifting toward this goal to expand the deployment of PV technologies and to increase the clean-energy share of the energy mix. TPV technologies rely on absorption of UV and/or IR light, while avoiding visible range absorption completely or as

---

A. J. Lopez-Garcia, V. Izquierdo-Roca, A. Pérez-Rodríguez
Institut de Recerca en Energia de Catalunya (IREC)
Jardins de les Dones de Negre, 1, 2ª pl, Sant Adrià del Besòs, 08930 Barcelona, Spain
E-mail: alopez@irec.cat

The ORCID identification number(s) for the author(s) of this article can be found under https://doi.org/10.1002/solr.202200928.

C. Voz, J. Puigdollers
Departament Enginyeria Electrònica
Universitat Politècnica Catalunya
c/Jordi Girona 3-1, 08034 Barcelona, Spain

J. M. Asensi
IN2UB
Departament de Física Aplicada
Universitat de Barcelona
Carrer de Martí i Franquès 1, 08028 Barcelona, Spain

A. Pérez-Rodríguez
IN2UB
Departament d'Enginyeria Electrònica i Biomèdica
Universitat de Barcelona
Carrer de Martí i Franquès 1, 08028 Barcelona, Spain

much as possible (selective and nonselective approaches).[2,3] These device concepts can potentially allow for nonintrusive implementation of transparent solar devices, as they will be essentially transparent to the human eye due to negligible absorption/emission of visible light, while harvesting wavelengths to which the human eye is blind.

Among the different approaches, inorganic technologies based on the use of oxide and chalcogenide materials have a strong interest because they are based on the use of stable, inexpensive, and earth-abundant materials that have a strong compatibility with industrial processes. Oxide materials for example have been extensively studied as UV-selective absorbers due to their wide bandgaps, and absorption onset close to the UV onset. This property leads to potentially highly transparent and color-neutral devices that exploit the UV photons of the solar spectra. Indeed, very high average visible transmission (AVT) values have been obtained with oxide-based transparent solar cells. (AVT is the measurement of how much light in the eye's photopic range is transmitted. Colour rendering index (CRI) is a measure, with values ranging from 0 to 100, of how well the color of an object is reproduced by comparing to a reference. Detailed descriptions of AVT and CRI and their relevance for TPV can be found in Refs. [2,4]). However, these devices have only achieved efficiencies of around 0.5% for the AM1.5G solar spectra limited by a low light utilization efficiency (LUE) value.[5–8] This parameter has been proposed in Ref. [2] as a relevant figure of merit for TPV technologies, and is defined by the product of the AVT and the photovoltaic conversion efficiency (PCE). Recently, new published works have shown that by embedding ultrathin a-Si:H layers in oxide-based devices, it was possible to increase significantly the PCE while maintaining high AVT and CRI values.[9–15]

In this work, transparent PV cells based on ultrathin intrinsic a-Si:H and oxide-based charge-transport layers (CTLs) are presented. The a-Si:H films have been studied in detail via optical characterization techniques including photothermal deflection spectroscopy (PDS) as well as UV–visible–near infrared (NIR) spectrophotometry. These techniques combined have allowed for a precise determination of the optical indices and absorption coefficient of the nanometric films. Full devices are presented afterward, showing record PCE and LUE values for this kind of TPV architecture. It is also shown that the performance of the TPV devices (in terms of AVT and PCE) can be tuned by subtle variation in the nanometric thickness of the a-Si:H film. Spectral response measurements confirmed that the devices preferentially absorb short wavelengths (i.e., $\lambda < 450$ nm) due to the ultrathin nature of the a-Si:H films, which frustrates most of the longer wavelength absorption. This is the desired behavior in this technology to enhance the transparency and aesthetic aspects of the TPV device.

2. Results and Discussion

In this work, TPV devices composed of planar inorganic ultrathin films have been fabricated using an architecture consisting of the intrinsic a-Si:H film coupled to oxide carrier-selective contacts at opposite interfaces (i.e., soda-lime glass (SLG)/fluorine-doped tin oxide (FTO)/ETL/a-Si:H/HTL/indium tin oxide (ITO)). FTO and ITO act as transparent electrodes and the nanometric intrinsic a-Si:H film works as the absorber layer. Aluminum-doped zinc oxide (AZO, 75 nm) is used as electron-transport layer (ETL) while molybdenum oxide (MoO$_3$, 10 nm) acts as the hole-transport layer (HTL). These transport layers allow for the extraction of electrons at the FTO electrode (cathode) and holes at the ITO electrode (anode), respectively (**Figure 1**). Both selective contacts, AZO and MoO$_3$, present wide bandgaps above 3.2 eV, thus greatly reducing unwanted parasitic absorption and allowing for increased transparency. Two different thicknesses of a-Si:H have been studied, 8 and 30 nm. Although the device structure does not use doped a-Si:H layers, its working mechanism is similar to a conventional p–i–n junction. In this sense, photogenerated carriers are collected first thanks to the electric field within the intrinsic layer and then filtered at the interfaces by the respective CTLs. In doping-free devices like these, the internal electric field builds on the different work function of the respective selective contacts.

We begin by analyzing the optical properties of the ultrathin a-Si:H films grown on quartz substrates and follow with a detailed optoelectronic characterization of the best prototype devices to extract the relevant TPV performance metrics (i.e., PCE, AVT, CRI, LUE) and to discuss the working mechanisms and features of these transparent devices.
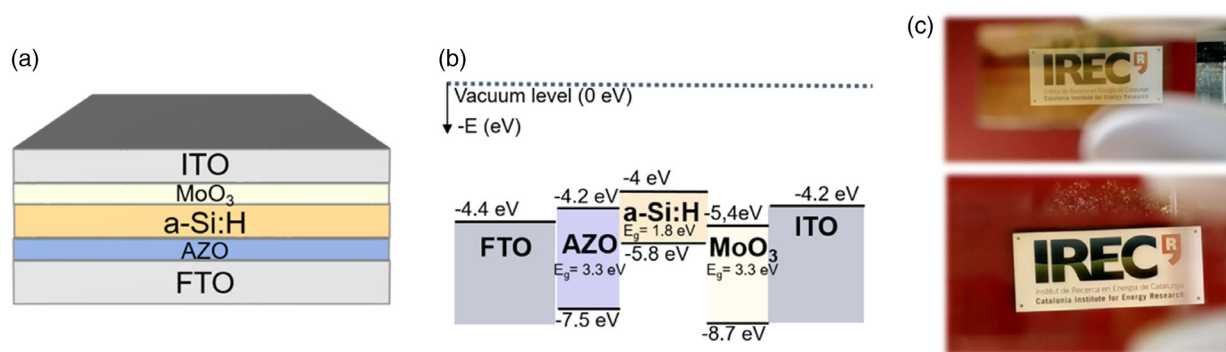

Figure 1. a) Schematic illustration of the transparent photovoltaic (TPV) device architecture (not to scale). b) Band diagram of the different films that conform the full device. c) Pictures of full (top) 30 nm device and (bottom) the 8 nm device, taken outdoors in broad daylight. The picture shows the TPV device, showing a white board with the IREC logo located at the building entrance.

2.1. Optical Characterization of Ultrathin a-Si:H Films

A prototypical inorganic UV–TPV device should ideally have its bandgap matched to the UV spectral onset (i.e., >2.8 eV), to neglect absorption of visible radiation. This equates to a rather natural wavelength selectivity toward UV harvesting. However, by using extremely thin absorbers with wide bandgap (as the case for a-Si:H), it is possible to mostly absorb UV light and some part of the blue-end spectral range. This occurs due to frustrated absorption engineered through the nanometric thickness, which simultaneously allows for higher transparency. However, devices will present some color even at high AVT values. If this is the case, it is possible to color tune the device to render it as color neutral as possible, for example, with interferometric filters or optical coatings.

Intrinsic a-Si:H films present a direct bandgap usually reported at values around 1.7–1.8 eV. It has also been reported to be extended up to 2.1 eV via quantum confinement, when thickness is reduced to the nanometric scale.[16] Additionally, previous work had shown that devices with 15 nm a-Si:H films presented a blueshifted absorption spectra, as compared to devices with 30 nm. This suggests a possible modification in the bandgap of a-Si:H in this thickness range.[10]

The PDS technique allows for an accurate measurement of the optical absorption in ultrathin a-Si:H films, which can confirm if there is any change in the bandgap as thickness is decreased. Together with spectrophotometry data, it also allows calculation of the optical bandgap and the Urbach. In this section, results on the characterization of a-Si:H ultrathin films are presented. For this, films of two different thicknesses have been assessed, corresponding to 8 and 30 nm (same as for the complete TPV devices). The a-Si:H films have been grown on quartz substrates, which have a flat transmittance profile within the UV–visible–NIR range.

Disordered and low crystallinity materials usually present band tails in the density of states that extend into the sub-band
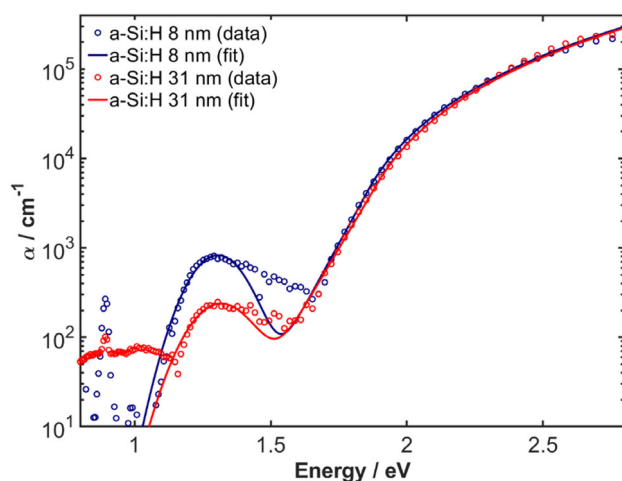
Table 1. Summary of parameters extracted from PDS measurements on a-Si:H films of 8 and 30 nm. The optical bandgap (E_g) the Urbach energy (E_u) for both films are presented.

Sample	α(2.5 eV) [cm^{-1}]	E_g [eV]	E_U [meV]
Quartz/a-Si:H (8 nm)	1.22×10^5	1.69	78
Quartz/a-Si:H (30 nm)	1.48×10^5	1.71	84

gap region, corresponding to localized states referred as Urbach front or Urbach tail.[17] These band tails are characterized by the Urbach energy (E_U), which can be interpreted as a measure of disorder in the material. The higher this value, the higher density of these states, which relates to poor semiconductor quality such as low lifetime and can have a strong impact in open-circuit voltage (V_{oc}).[18] PDS allows for an accurate determination of this value. **Figure 2** shows the experimental absorption coefficient for both a-Si:H films (8 and 30 nm). The absorption coefficient of the films exceeds 10^5 for wavelengths above 2.5 eV. Additionally, a sub-band gap contribution, below 1.7 eV, is observed in both cases. This sub-band gap contribution could be related to recombination dynamics in the material and localized surface defect states (see Supporting Information). From the experimental absorption coefficient values $\alpha(E)$ and using the Cody optical model, the value of the optical bandgap can be calculated with great precision.[19,20] In both cases, the optical value was found to be of 1.69 and 1.71 eV for the 8 and the 30 nm film, respectively (**Table 1**). This value indicates that at these nanometric thickness values, the bandgap still behaves "classically" and there is no indication of any shift in the bandgap due to quantum confinement.

To extract the numerical value for the Urbach energy, Equation (1) is used, where α_0 and U_1 are constants determined through fitting the data from $\alpha(E)$, h is Planck's constant and ν is the frequency of the incident radiation. Thus, plotting $\ln(\alpha)$ as a function of energy and calculating the inverse of the slope yield the sought value for the Urbach energy E_U

$$\alpha(h\nu) = \alpha_0 \cdot e^{\left(\frac{h\nu - U_1}{E_U}\right)} \tag{1}$$

The Urbach energy was calculated for both a-Si:H film thicknesses, yielding a similar value of around 80 meV. This value is relatively higher than the 50 meV typically measured in thick (200–300 nm) state-of-the-art a-Si:H films.[21,22] This can be explained considering the higher contribution of surface states in the ultrathin a-Si:H layers. A higher E_U value can introduce some V_{oc} loss, which makes interface passivation an important aspect to improve TPV devices.

2.2. Optical Characteristics and J–V Characteristics of a-Si:H/Oxide TPV Devices

In this section, complete device structures are characterized by measuring their transmittance by optical spectrophotometry. Complete devices were fabricated with two sets of samples, including 8 and 30 nm a-Si:H absorber layers while leaving the rest of the structure unchanged (i.e., AZO and MoO$_3$ fixed

Figure 2. Absorption coefficient of a-Si:H films of 8 and 30 nm extracted from photothermal deflection spectroscopy (PDS) measurements. Solid circles are the experimental values, and solid lines are the fit to the model described in Supporting Information by Equations S(1), S(2), and S(3) (see also Figure S1 and Table S1 in Supporting Information).
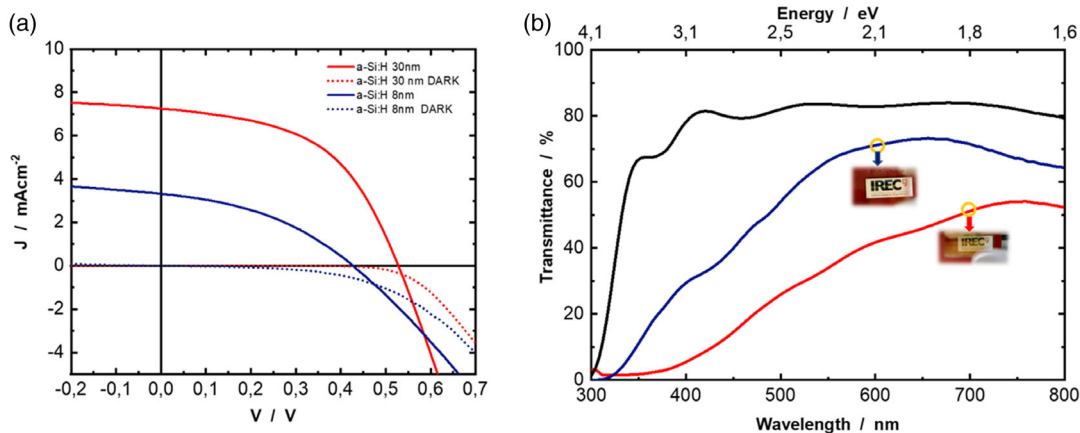
Figure 3. TPV characterization of best devices. a) Current voltage–density (J–V) characteristics measured under AM1.5G illumination of SLG/FTO/AZO(75 nm)/a-Si:H(8, 30 nm)/MoO$_3$(10 nm)/ITO. b) Transmittance spectra of devices shown in (a). Transmittance of the SLG/FTO substrate is shown as reference (black curve).

to 75 and 10 nm, respectively). These measurements allow for the determination of the transmittance spectra of the complete TPV devices, which will serve as input for the calculation of the TPV figures of merit of AVT and CRI. Afterward, the study of the current density–voltage (J–V) characteristics measured in dark and under AM1.5G illumination is presented.

Figure 3 presents the transmittance spectra from 300 to 800 nm of the complete devices extracted from the spectrophotometry measurements. The SLG/FTO substrate transmittance is also presented as a reference. For both a-Si:H thicknesses, the transmittance in the visible range is quite high, showing an expected increase in transmittance for the sample with a thinner 8 nm a-Si:H layer. From these spectra, the AVT and CRI figures of merit are calculated (**Table 2**). The AVT parameter weighs in the photopic response of the human eye, which sensitivity is centered around the green (550 nm). A notable difference between both samples is observed when calculating the AVT and CRI values, showing the possibility of tuning the aesthetics of the device with changes in the thickness of the a-Si:H layer. The thinner device (8 nm) presents a very high value of AVT = 66%, in fact the highest AVT reported so far for these materials and architecture, and comparable to reported UV selective TPV pure oxide devices.[8–10] The AVT values drop to AVT = 35.4% for the thicker devices (30 nm), though still being quite transparent. As for the CRI parameter, the thinner devices present again higher values. For the 8 nm device, the CRI is as

high as CRI = 85, while for the 30 nm case, it shows a value of CRI = 75 resulting in a less color-neutral device. Another notable feature is the UV filtering capabilities of these devices, which is convenient to eliminate unwanted and potentially harmful wavelengths. This added functionality is especially interesting, for example, in smart window applications that include an IR selective organic solar cell in addition to the UV–blue selective device, leading to a tandem-like device architecture.[23] In this device architecture, filtering of the UV radiation by the inorganic top cell is relevant to prevent potential degradation of the bottom IR organic cell.

The device with 30 nm a-Si:H layer absorbs almost all the UV radiation evidencing excellent UV-filtering capabilities. However, the 8 nm device is less efficient at this task and still transmits a noticeable amount of this radiation. Absorption in this UV region increases exponentially with the thickness of the a-Si:H layer.

Resuming with the optoelectronic characterization, J–V characteristics in dark and under AM1.5G illumination of the best devices are presented in Figure 3 and PV parameters are presented in Table 2. Statistics on the devices are presented in Figure S2, Supporting Information, presenting box plots of the devices with either a-Si:H film thickness. Measurements were made from −0.2 to 0.7 V, thus including the three quadrants. No hysteresis in the electrical characteristics was observed either sweeping from negative to positive potential or vice versa. The 30 nm device presents a PCE of 1.95% while the 8 nm film presents a still remarkable PCE = 0.56% for a TPV device. This is the highest PCE value reported so far for oxide-based TPV devices. In general, there is an overall improvement in all PV parameters for the 30 nm device as compared to the 8 nm one. In terms of J_{sc}, its value is more than doubled, which can be clearly associated to the increased absorption and subsequent photogeneration. Both the FF and V_{oc} values are also significantly higher for the 30 nm device. The relative increase in FF for the 30 nm device is thought to come from the increased photocurrent, which brings the solar cell to an operation point less influenced by parasitic resistances. The V_{oc} of 0.528 V for the thick device is also

Table 2. Summary of results with TPV parameters of fabricated devices presented in Figure 3.

TPV device architecture	CRI	AVT [%]	V_{oc} [V]	J_{sc} [mAcm^{-2}]	FF [%]	PCE [%]	LUE [%]
FTO/AZO/a-Si:H(8 nm)/MoO$_3$/ITO	87	66.0	0.427	3.30	39.4	0.56	0.4
FTO/AZO/a-Si:H(30 nm)/MoO$_3$/ITO	75	35.4	0.528	7.24	51.0	1.95	0.7

significantly higher compared to the $V_{OC} = 0.427$ V measured for the 8 nm device. It is worth noting that a V_{oc} deficit is observed in both devices, since state-of-the-art a-Si:H p–i–n solar cells have reached values of around 0.9 V.[24–26] Such deficit of V_{oc} is quite important and hence constitutes an aspect to tackle to increase the potential of these TPV devices. For instance, interface recombination losses are expected to be much more relevant for ultrathin PV devices. Additionally, in this work, we use transparent oxide-based selective contacts replacing the highly doped layers of traditional p–i–n a-Si:H solar cells. The V_{oc} value finally results from the quasi-Fermi level splitting (QFLS) at the opposite interfaces (selective contacts). If the work functions of the respective selective contacts are misaligned with respect to the conduction and valence bands of the a-Si:H layer, a transport barrier will be created and will lead to QFLS reduction and hence of V_{oc}. With this in mind, finding suitable selective contacts that are optically transparent in the targeted absorption range is very important for improving the overall performance of these devices.

In contrast, when comparing the J–V characteristics in dark versus under AM1.5G illumination, a cross-over effect is observed in both types of device. This effect has been ascribed either to the presence of a light-dependent barrier or to changes in conductivity of the a-Si:H (i.e., increased photoconductivity).[27] To deepen in the knowledge of the potential loss mechanisms of the TPV devices, the J–V curves have been fitted using the 1-diode model for a solar cell equivalent circuit, using the "2–3 diode fit" software.[28,29] The extracted parameters from the fitting are shown in Table S3, Supporting Information. The 30 nm device presents a high shunt resistance value in the order of 10^4 Ωcm^2 confirming high conformality of the films across the device and the absence of relevant shunting paths. On the contrary, for the device with an 8 nm thick a-Si:H layer, the shunt resistance is one order of magnitude less, around 10^3 Ωcm^2. This suggests in this case a poorer level of conformality and coverage of the nanometric layers in the device architecture. When looking at the series resistance values, the results are in the same order of magnitude, yet still higher for the 8 nm device (11 Ωcm^2 for the 30 nm device and 41 Ωcm^2 for the 8 nm device). The relatively high series resistance most probably

comes from the wide-bandgap oxide hole-selective contact and the resistance of the TCOs used as transparent electrodes. As for the ideality factor, the values obtained in both types of devices are close or slightly above 2, suggesting that the main recombination pathways are associated to interface recombination. This agrees with the ultrathin nature of the films, as bulk recombination losses are not expected in such device architectures. These results again highlight the relevance of the interfaces in the device performance.[30] In this sense, optimization of the band alignment at the interfaces as well as increasing interface defect passivation are relevant features to achieve an improvement in overall device performance.

Concluding the optoelectronic characterization, J–V measurements under different light intensities were carried out applying various neutral density filters after the AM1.5G illumination (Figure S3, Table S2, Supporting Information). Plotting the short-circuit current density as a function of light intensity can serve as a tool for checking if monomolecular recombination or bimolecular recombination dominate in the device. From 20 to 100 mW cm^{-2} of power density, the data shows linear dependency, indicating that monomolecular recombination is the dominant mechanism.[30]

Summarizing the optical and optoelectronic characterizations, the device with a thicker a-Si:H layer (30 nm) presents an AVT = 35.4%, CRI = 75, and PCE = 1.95%, yielding a LUE = 0.7%. For the thinner device with 8 nm a-Si:H film, the respective parameters are AVT = 66.0%, CRI = 85, and PCE = 0.56%, yielding an LUE = 0.4%. The thinner sample excels in transparency and color neutrality, while the thicker sample shows the higher LUE and PCE values reported so far for this kind of devices. These results highlight that differences in the thickness of the layers have much higher impact in TPV technologies as compared to conventional opaque PV.

2.3. Spectral Response

Spectral response measurements were performed on both 8 and 30 nm a-Si:H devices to compare and analyze their response (**Figure 4**a). The external quantum efficiency (EQE) maximum
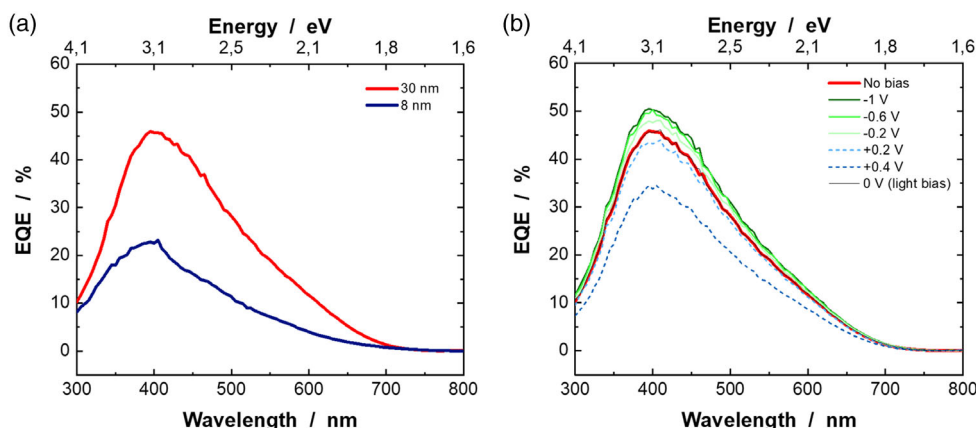
Figure 4. a) Comparison of external quantum efficiency (EQE) of device with 30 nm a-Si:H film and a device with 8 nm a-Si:H film. b) EQE extracted from spectral response measurements on a device with a-Si:H film of 30 nm. EQE is shown with no bias, with white light bias and at different negative electrical biases from +0.4 to −1 V.

is located at 400 nm in both cases in their respective EQE spectra, showing a steep drop in response toward lower photon energies. As expected, the spectral response of the thinner 8 nm device is lower than for the 30 nm device, but presents a similar profile across the spectral range. This behavior supports that the UV–blue selective absorption responds to the ultrathin nature of the films, which results in a frustrated long wavelength absorption. It is also worth noting that wavelength-selective behavior is not always observed with ultrathin absorber materials. As example, in Ref. [31], ultrathin CIGS devices are presented exhibiting a "flat" EQEs across the whole range from 300 nm to the wavelength corresponding to the energy bandgap of CIGS, showing transparency, but also leveled broadband photoresponse.

In Figure 4b, a detailed analysis on the EQE of the best device at different light and electrical biases is presented. Under either conditions (i.e., with or without electrical bias), the maximum EQE is still located at 400 nm. The spectrum obtained under no light exposure remains almost identical as the one under uniform white light, which indicates good carrier collection irrespectively of bulk illumination. When applying increasingly negative electrical biases, there is a slight enhancement in quantum efficiency of the TPV device. The small change suggests that most of the photogenerated carriers in the a-Si:H absorber reach the interfaces with the CTLs. The relative increase, as compared with the spectra of the device under no electrical bias, is most notable near the EQE peak and almost negligible at wavelengths longer than 450 nm, suggesting improved photocarrier collection mainly near the front interface. The EQE noticeably degrades for positive bias voltages, as it could be expected for the dominant drift-assisted carrier collection in this device architecture. This reduction at high bias could also be an indication of the existence of some transport barrier at the CTL/a-Si:H interfaces. To confirm that no overestimation of J_{sc} has been done, a photon balance check is presented in Figure S4.

3. Conclusion

We have studied the potential of nanometric intrinsic a-Si:H/oxide structures for TPV applications in a metal-free device architecture including transparent conductive oxides as electrical contacts. The optical properties of the ultrathin a-Si:H films have been experimentally determined by spectrophotometric measurements and the Urbach energy of ultrathin a-Si:H absorbers has been determined. Spectral response and optoelectronic measurements have proved a preferential absorption of short wavelengths (UV–blue) from the solar spectra while still presenting high AVT values, comparable to those of full oxide UV-selective devices. The reported devices present a record efficiency of PCE = 2% and AVT = 35.4% (LUE = 0.7%) and PCE = 0.6% and AVT = 66% (LUE = 0.4%) with a 30 and 8 nm a-Si:H film, respectively. Use of substrates with sizes up to $5 \times 5 \, cm^2$ has allowed to achieve good statistics to analyze the reproducibility of the results when working with 0.07 cm^2 active area devices that have been defined using a metallic shadow mask during ITO deposition. A first attempt for process upscaling has also been done with the fabrication of a $5 \times 5 \, cm^2$ solar cell. However, even in this case, the devices show a dramatic drop in the device efficiency to values lower than 0.1%. This is likely mainly related to

the high series resistance of the ITO front contact, which determines a drastic loss in device efficiency. This implies the need for a redesign of the fabrication process when using higher area devices and possibly the introduction of a metallic grid with finger thicknesses of around 100 μm, which could allow to have a nonintrusive grid for efficient carrier collection. Nonetheless, we have demonstrated the potential of the technology using smaller active area, which allowed avoiding these resistive and parasitic losses when upscaling. The results detailed in this work represent a great improvement as compared to state-of-the-art devices with similar architectures. To further improve these TPV devices, it is necessary to optimize their architecture by paying special attention to the interfaces. These structures show a promising route for opening alternative PV applications with seamless integration. Applications of this technology can potentially include BIPV, VIPV, APV, low-power demand applications such as powering future internet of things devices and as self-powered light sensors. The TPV devices present multifunctional capabilities, such as good UV filtering, that add up to the PV effect. To conclude, it is worth noting that all materials and processes used in this work are scalable and compatible with existing and established industries, using low process temperatures as well as earth-abundant, stable, and low-cost materials, which are also key features to have a future deployment of such technologies at an industrial level.

4. Experimental Section

Sample Preparation: The solar cells fabricated in this work presented the structure SLG/FTO/AZO/a-Si:H(8, 30 nm)/MoO$_3$/ITO with active area of 0.07 cm^2. Commercial SLG/FTO substrates (Merck; $R_{sh} = 10 \, \Omega sq^{-1}$) were used as substrate and transparent back-contact for the solar cell devices. Substrates were rinsed in distilled water, dried in Ar flux, and afterward cleaned by subsequent ultrasonic baths in isopropanol and ultrapure H$_2$O at room temperature for 10 min each. Afterward, the substrates were dried in Ar flux and finally submitted to a 5 min O$_3$ treatment. A 75 nm AZO film was grown in an atomic layer deposition (ALD) system (Savannah S200, Cambridge Nanotech) at 135 °C. The precursors used are diethylzinc (DEZ 95%, STREM), ultrapure H$_2$O and trimethylaluminium (TMA 99%, STREM) and using N$_2$ as purging gas, with a DEZ:TMA ratio of 19:1. 21 supercycles were performed with 19 H$_2$O/N$_2$/DEZ/N$_2$ (20 ms/3 s/15 ms/3 s) cycles and 1 H$_2$O/N$_2$/TMA/N$_2$ (50 ms/1 s/20 ms/5 s) cycle. Afterward, intrinsic a-Si:H ultrathin films of 8 and 30 nm were deposited by plasma-enhanced chemical vapor deposition (PE-CVD) (Elettrorava) with an radio frequency (RF) power supply of 13.56 MHz at 6 W. Substrate temperature was measured at 220–250 °C during deposition, with a mixed 36/12 sccm SiH$_4$/CH$_4$ atmosphere and with deposition times of 1 and 4 min, respectively (thickness calibration has been determined by means of a profilometer) (KLA Tencor D-120), studying films with varying deposition times. Additionally, thin layers comparable to the ones studied in this work were characterized by high-resolution transmission electron microscopy (HRTEM) at the advanced microscopy laboratory (Laboratorio de Microscopia Avanzada (LMA), Universidad de Zaragoza). The deposition rate for the conditions used in this work was about 1.3 Å s^{-1}. MoO$_3$ films of 10 nm were deposited by thermal evaporation (Oerlikon Univex 250) using raw MoO$_3$ powder (99.995%, Alfa Aesar) as evaporant in a tungsten boat. The chamber was evacuated to a base pressure of 10^{-6} mbar before evaporation and the deposition took place at room temperature at a rate of 0.3 Å s^{-1} as measured with a Ag-coted 6 MHz quartz crystal microbalance (Inficon SQC-310). To complete the device, a 190 nm ITO film working as front contact was deposited by DC-Pulsed Confocal Magnetron Sputtering (Alliance CT-100). Before deposition, the chamber was evacuated at 10^{-7} mbar and the substrate

was heated up to 200 °C. The ITO target (Neyco; In_2O_3/SnO_2 90/10 wt%, 4 N) was pre-sputtered with a shutter in closed configuration to remove any surface contaminants. The deposition took place at a working pressure of 3×10^{-3} mbar in a mixed 30/0.5 sccm Ar/O_2 atmosphere, applying a DC power density of 1.9 W cm^{-2} to the target.

Characterization: The optical absorption of quartz/a-Si:H samples was characterized by PDS. A single-slab model was applied to compute the absorption coefficient. The transverse PDS setup used in this work consisted of a 100 W tungsten halogen lamp, PTI 01-0002 monochromator (two-grating monochromator, spectral range of 400–2000 nm), and Thorlabs MC1000 optical chopper (4 Hz light modulation frequency). A Signal Recovery 7265 lock-in amplifier was connected to a Hamamatsu C10442-02 position-sensitive detector (Hamamatsu C10442-02 PSD) to measure the deflection of an MC632C 10 mW laser probe beam. Samples were put in a quartz cell filled with Fluorinert TM FC-40. A personal computer was used to control the monochromator, change the order filters, and store the PDS signal read from the lock-in amplifier.[32]

Spectrophotometry measurements were acquired with a UV–visible– NIR spectrophotometer (Perkin Elmer Lambda L950) with an integrating sphere and in single-beam setup, in transmittance and reflectance mode with spectral range from 300 to 800 nm to measure the completed device total transmittance and reflectance. This data was also used to calculate the device AVT and CRI.

J–V measurements under illumination were carried out using a class AAA solar simulator with AM1.5G illumination calibrated using an NREL-certified Si reference solar cell (Abet Technologies Model 15150). Electrical measurements were carried out with a source–measure unit (Keithley SMU 2400) in 4-wire sense mode, remotely controlled by the software Tracer (ReRa solutions) using an IEEE 488 GPIB Instrument Control Device (National Instruments GPIB-USB-HS). Spectral response measurements were acquired using a spectral response system (Bentham PVE300) calibrated with Si and Ge photodiodes. For optoelectronic measurements, the samples were placed in a dark opaque matt to avoid any back reflections that could alter the characterization of the transparent solar cells.

Supporting Information

Supporting Information is available from the Wiley Online Library or from the author.

Conflict of Interest

The authors declare no conflict of interest.

Data Availability Statement

The data that support the findings of this study are openly available in Zenodo repository at http://doi.org/10.5281/zenodo.7215223.

[1] G. Masson, I. Kaizuka, can be found under, https://iea-pvps.org/wp-content/uploads/2020/02/5319-iea-pvps-report-2019-08-lr.pdf (accessed: October 2022).

[2] C. J. Traverse, R. Pandey, M. C. Barr, R. R. Lunt, *Nat. Energy* **2017**, *2*, 849.

[3] R. R. Lunt, *Appl. Phys. Lett.* **2012**, *101*, 43902.

[4] C. Yang, D. Liu, M. Bates, M. C. Barr, R. R. Lunt, *Joule* **2019**, *3*, 1803.

[5] R. Karsthof, P. Räcke, H. Von Wenckstern, M. Grundmann, *Phys. Status Solidi A* **2016**, *213*, 30.

[6] M. Patel, H. Kim, J. Kim, J. Yun, E. Ha, H. Park, *Sol. Energy Mater. Sol. Cells* **2017**, *170*, 246.

[7] D. K. Ban, M. Patel, T. T. Nguyen, J. Kim, *Adv. Electron. Mater.* **2019**, *5*, 1900348.

[8] A. J. Lopez-Garcia, A. Bauer, R. Fonoll Rubio, D. Payno, Z. Jehl Li-Kao, S. Kazim, D. Hariskos, V. Izquierdo-Roca, E. Saucedo, A. Pérez-Rodríguez, *Sol. RRL* **2020**, *4*, 2000470.

[9] S. Kim, M. Patel, T. T. Nguyen, J. Yi, C. P. Wong, J. Kim, *Nano Energy* **2020**, *77*, 105090.

[10] A. J. Lopez-Garcia, O. Blazquez, C. Voz, J. Puigdollers, V. Izquierdo-Roca, A. Pérez-Rodríguez, *Sol. RRL* **2022**, *6*, 2100909.

[11] M. Patel, J. H. Seo, T. T. Nguyen, J. Kim, *Cell Rep. Phys. Sci.* **2021**, *2*, 100591.

[12] S. Kim, J. Yi, J. Kim, *Sol. RRL* **2021**, *5*, 2100162.

[13] M. Patel, S. Kim, T. T. Nguyen, J. Kim, C.-P. Wong, *Nano Energy* **2021**, *90*, 106496.

[14] M. Patel, V. Vitthal Satale, S. Kim, K. Lee, J. Kim, *J. Power Sources* **2022**, *548*, 232009.

[15] S. Kim, M. Patel, T. T. Nguyen, N. Kumar, P. Bhatnagar, J. Kim, *ACS Appl. Mater. Interfaces* **2022**, *14*, 706.

[16] Y. Abdulraheem, I. Gordon, T. Bearda, H. Meddeb, J. Poortmans, *AIP Adv.* **2014**, *4*, 057122.

[17] F. Urbach, *Phys. Rev.* **1953**, *92*, 1324.

[18] J. Chantana, Y. Kawano, T. Nishimura, A. Mavlonov, T. Minemoto, *Sol. Energy Mater. Sol. Cells* **2020**, *210*, 110502.

[19] G. D. Cody, in *Semiconductors and Semimetals* (Eds: J. I. Pankove), Vol. *21*, Elsevier, Amsterdam, Netherlands **1984**, pp. 11–82, Chapter 2.

[20] T. M. Mok, S. K. O'Leary, *J. Appl. Phys.* **2007**, *102*, 113525.

[21] K. Higuchi, K. Tabuchi, K. S. Lim, M. Konagai, K. Takahashi, *Jpn. J. Appl. Phys.* **1991**, *30*, 1635.

[22] V. Dalal, R. Knox, B. Moradi, *Sol. Energy Mater. Sol. Cells* **1993**, *31*, 349.

[23] A. Pérez-Rodríguez, in *presented in NEXTGEN, 19: 2019 Next Generation High Efficiency Photovoltaics Int. School and Workshop*, Mallorca, October **2019**.

[24] T. Matsui, K. Maejima, A. Bidiville, H. Sai, T. Koida, T. Suezaki, M. Matsumoto, K. Saito, I. Yoshida, M. Kondo, *Jpn. J. Appl. Phys.* **2015**, *54*, 08KB10.

[25] M. Stuckelberger, R. Biron, N. Wyrsch, F.-J. Haug, C. Ballif, *Renewable Sustable Energy Rev.* **2017**, *76*, 1497.

[26] K. Belrhiti Alaoui, S. Laalioui, Z. Naimi, B. Ikken, A. Outzourhit, *AIP Adv.* **2020**, *10*, 095315.

[27] S. S. Hegedus, W. N. Shafarman, _Prog. Photovoltaics Res. Appl._ **2004**, _12_, 155.

[28] S. Suckow, T. M. Pletzer, H. Kurz, _Prog. Photovoltaics Res. Appl._ **2014**, _22_, 494.

[29] G. Yue, B. Yan, C. Teplin, J. Yang, S. Guha, _J. Non-Cryst. Solids_ **2008**, _354_, 2440.

[30] S. Ryu, D. C. Nguyen, N. Y. Ha, H. J. Park, Y. H. Ahn, J.-Y. Park, S. Lee, _Sci. Rep._ **2019**, _9_, 19846.

[31] M. Jeong Shin, A. Lee, J. Hyung Park, A. Cho, S. Kyu Ahn, D. Shin, J. Gwak, J. Ho Yun, J. Yoo, J.-S. Cho, _Nano Energy_ **2022**, _92_, 106711.

[32] J. Serra, J. Andreu, G. Sardin, C. Roch, J. M. Asensi, J. Bertomeu, J. Esteve, _Phys. B Condens. Matter_ **1991**, _170_, 269.